Electronic Supplementary Information

Ultra-small Fe_3O_4 nanodots encapsulated in layered carbon nanosheets with fast kinetics for lithium/potassium-ion battery anodes

Qianqian Peng,[a†] Chuan Guo,[a†] Shuo Qi,[a] Weiwei Sun,[a] Li-Ping Lv,[a] Fei-Hu Du,[a] Baofeng Wang,[b] Shuangqiang Chen,[a*] Yong Wang[a*]

[a] *Department of Chemical Engineering, School of Environmental and Chemical Engineering, Shanghai University, 99 Shangda Road, Shanghai, P. R. China, 200444. Email: chensq@shu.edu.cn; yongwang@shu.edu.cn; Tel: +86-21-66136598*

[b] *Shanghai Key Laboratory of Materials Protection and Advanced Materials in Electric Power, Shanghai University of Electric Power, Shanghai 200090, China.*

(† The authors contributed to this work equally)

Figures and Tables

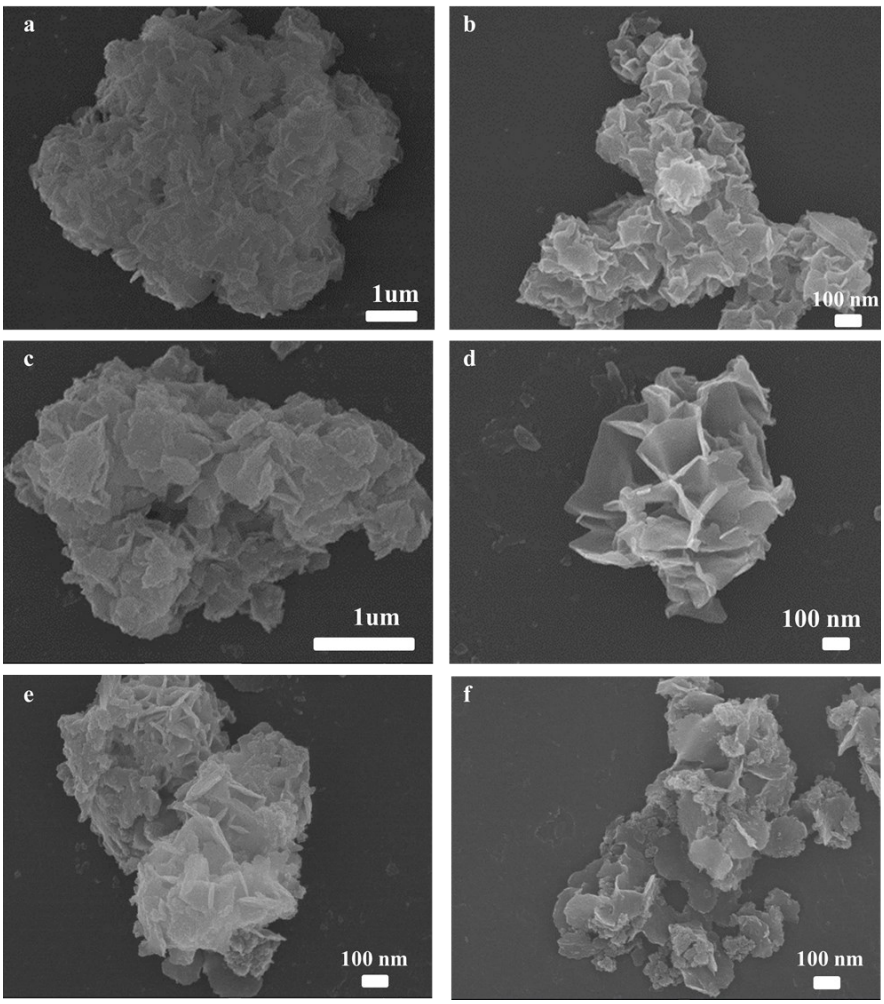

Fig. S1 SEM images of (a and b) Fe-coordination compound; (c and d) Fe_3O_4@LCS-400; (e and f) Fe_3O_4@LCS-600

Table S1 Elemental analysis of Fe_3O_4@LCS-(400/500/600) nanocomposites

Samples	Elemental contents (wt. %)			
	O	C	H	Fe
Fe_3O_4@LCS-400	21.31	21.74	1.13	55.82
Fe_3O_4@LCS-500	21.54	20.83	1.24	55.99
Fe_3O_4@LCS-600	22.25	19.04	0.45	58.26

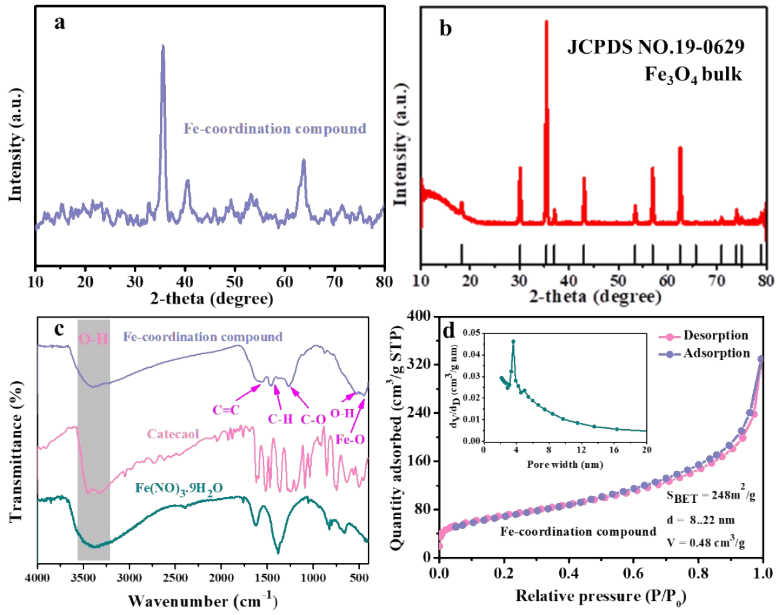

Fig. S2 XRD patterns of (a) Fe-coordination compound and (b)Fe_3O_4 bulk, (c) FTIR curves of Fe-coordination compound, catechol and $Fe(NO)_3 \cdot 9H_2O$, (d) Nitrogen adsorption-desorption isotherms and plots for the pore-size distribution of Fe-coordination compound.

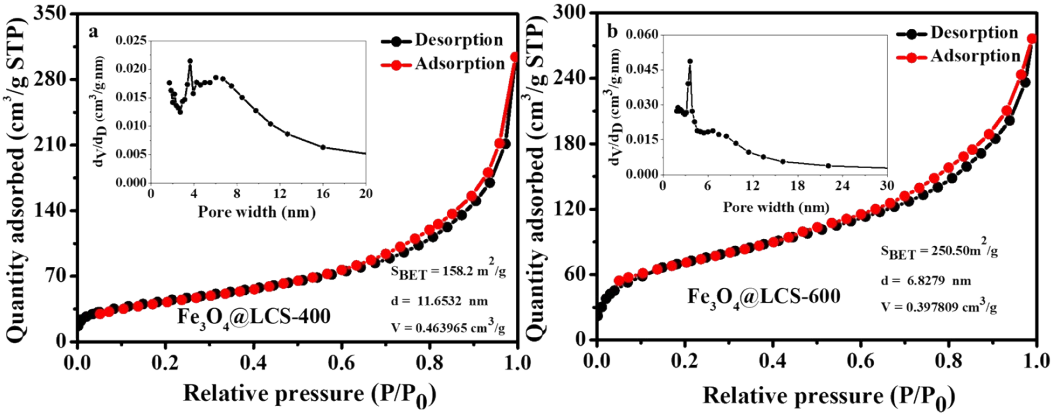

Fig. S3 Nitrogen absorption isotherm and the corresponding average pore size distribution of (a) Fe_3O_4@LCS-400; (b) Fe_3O_4@LCS-600

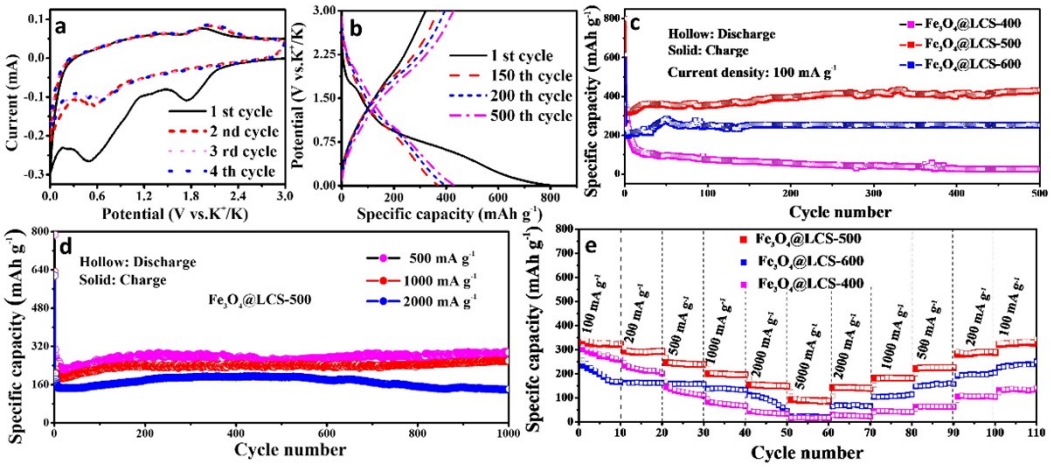

Fig. S4. The electrochemical performances of Fe_3O_4@LCS-500 electrode as the anode of KIBs: (a) CV curves in the first four cycles at 0.1 mV s^{-1}. (b) charge/discharge profiles at 100 mA g^{-1}. (c) Cycling performance of Fe_3O_4@LCS-400/500/600 at 100 mA g^{-1}. (d) Cycling performances of Fe_3O_4@LCS-500 at current densities of 500, 1000, and 2000 mA g^{-1}, respectively. (e) The rate performances of Fe_3O_4@LCS-(400/500/600) electrodes at various current densities.

To examine the possibility of application in KIBs, Fe_3O_4@LCS-500 nanocomposites were measured *via* similar electrochemical techniques as LIBs. Cycle voltammetry was applied to analyze the potentials of K^+ ion's insertion/extraction properties in Fig. S4a. Fig. S4b presents charge/discharge behaviors of the Fe_3O_4@LCS-500 electrode at 100 mA g^{-1}, exhibiting a rechargeable capacity of 321.2 mAh g^{-1} with a Coulombic efficiency of 40%, and a discharge plateau at ~0.55 V in the first cycle. The largely irreversible capacity loss is ascribed to the formation of the SEI layer, irreversible carbon storage, and the decomposition of the electrolyte. Cycling performances of Fe_3O_4@LCS-(400/500/600) electrodes are shown in Fig. S4c. Fe_3O_4@LCS-500 electrode maintained a reversible capacity of 429.7 mAh g^{-1} after 500 cycles. By contrast, the reversible capacities of Fe_3O_4@LCS-400 and Fe_3O_4@LCS-600 were only 24.5 and 250.5 mAh g^{-1} after 500 cycles, respectively. And the Fe_3O_4 bulk electrode delivered a reversible capacity of 36.9 mAh g^{-1} as shown in Fig. S9a**.** Specifically, Fe_3O_4@LCS-500 electrode has exhibited good rate capacities of 286.8, 260, and 141.1 mAh g^{-1} at current densities of 500, 1000, and 2000 mA g^{-1}, respectively. To demonstrate the rate capability, Fe_3O_4@LCS-(400/500/600) electrodes were further tested at different current densities of 100, 200, 500, 1000, and 2000 mA g^{-1} in Fig. S4e. With the advantages of ultra-small Fe_3O_4 nanodots, high surface area, thin and mesoporous carbon

layers, Fe_3O_4@LCS-500 electrode has delivered high reversible capacities of 340, 330, 294, 246, and 201 mAh g^{-1}, respectively. When the current density was returned to 100 mA g^{-1}, the capacity of Fe_3O_4@LCS-500 electrode reached 321 mAh g^{-1}, close to the initial reversible capacity, which is highly ascribed to the short potassium pathway among Fe_3O_4 nanodots, high surface area, and fast potassium diffusion coefficient. In contrast, Fe_3O_4@LCS-(400/600) electrodes and the Fe_3O_4 bulk electrode (Fig. S9b) exhibited slightly poor rate capabilities, which were probably ascribed to high internal resistance and low electronic conductivity.

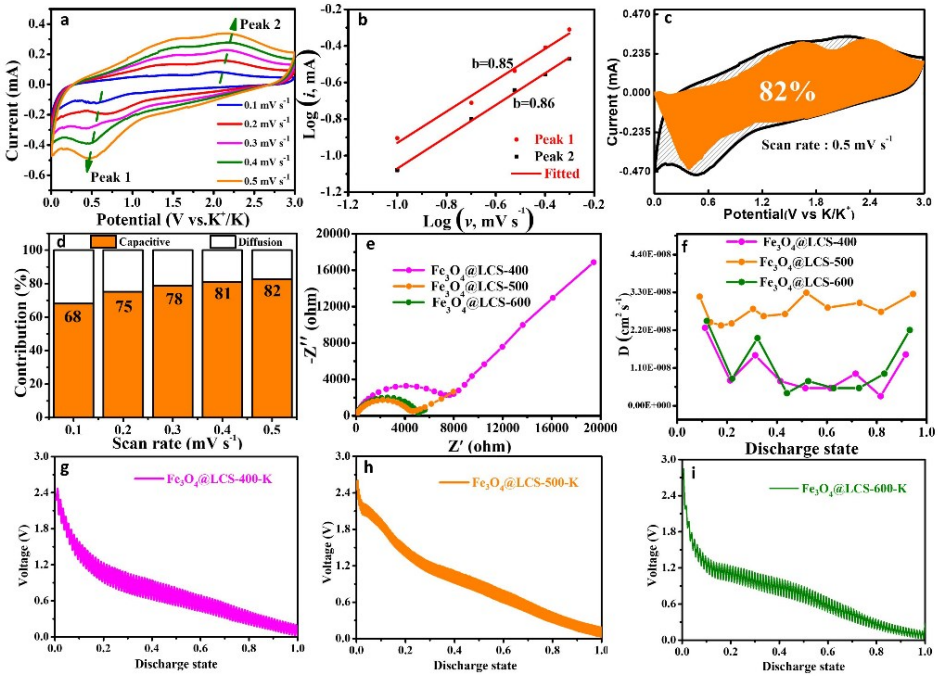

Fig. S5. Capacity contribution and potassium diffusion coefficients of Fe_3O_4@LCS-500 for KIB's anode : (a) CV curves at different scan rates from 0.1 to 0.5 mV s^{-1}; (b) b value with linear relationship between log(i) and log(v); (c) capacitive contributions at 0.5 mV s^{-1}; (d) contribution ratio of capacitive–controlled behaviors at various scan rates; (e) the Nyquist plots and (f) chemical diffusion coefficients of K^+ ions in different electrodes and (g-i) GITT curves of Fe_3O_4@LCS-(400/500/600) electrodes.

To quantify the potassium diffusion coefficient and capacitive controlled behavior, CV curves at various scan rates, ranging from 0.1 to 0.5 mV s^{-1}, were investigated. The CV curves show similar shapes in Fig. S5a, but exhibit increased intensities of anodic and cathodic peaks as scan rates are increasing. Similar investigations about capacity contribution between capacitive and diffusion-

controlled behaviors are adopted as that of LIBs. Based on the CV curves and the above-mentioned equations, the b values, the slops of the fitted plots in Fig. S5b, were calculated to be 0.85 and 0.86, respectively, illustrating dominated capacitive controlled behavior. Regarding to the two-type b value for LIBs and one-type for KIBs, the Li cations can adequately react with Fe_3O_4 and reversibly during cycles, but K cations can only fully react with Fe_3O_4 in the first discharge process, leaving a high irreversible capacity loss, which can be demonstrated by their initial Coulombic efficiencies of 65.76% for LIBs and 40% for KIBs. Therefore, LIBs are mainly dominated by diffusive behaviors during discharge and capacitive behavior during charge, yet KIBs are only displaying the capacitive behavior during charge and discharge, namely K cations are only reacted with Fe_3O_4 on the surface after the first discharge process. In Fig. S5c, the portion of capacitive contribution at 0.5 mV s^{-1} of Fe_3O_4@LCS-500 electrode was 82%. The contribution ratio is also different if the applied current density is changed. As shown in Fig. S5d, about 68% of the total capacity comes from surface capacitance at a low scan rate of 0.1 mV s^{-1}. This value is gradually increased to 75%, 78%, 81% and 82%as the scan rate is increased to 0.2, 0.3, 0.4 and 0.5 mV s^{-1}, respectively. Note that the capacitive-controlled and diffusion-controlled contributions have coexisted at both low and high current densities. Based on the calculated contribution ratios, it is easy to deduce that the diffusion coefficient highly affects the capacity contribution meaning that capacitive-controlled behavior takes the lead at fast scan rates and diffusion-controlled behavior at low scan rates. The electrochemical resistances are measured by the EIS technique in Fig. S5e for a better comparison of interfacial resistance, charge transfer, and ionic conductivity. The depressed semi-circle in the high electronic conductivity. To quantify the diffusion coefficient value of K cations, GITT was applied. Assuming the ionic conductive transfer of K^+ satisfies the Fick's second law, diffusion coefficients can be calculated based on the GITT results (Fig. S5f-i). The diffusion coefficient of K cations of the Fe_3O_4@LCS-500 electrode is around $1.06*10^{-8}$ cm^2 S^{-1}, which is much higher than that of Fe_3O_4@LCS-400 ($8.2*10^{-9}$ cm^2 S^{-1}) and Fe_3O_4@LCS-600 ($8.9*10^{-9}$ cm^2 S^{-1}), implying fast diffusion coefficient in Fe_3O_4@LCS-500 electrode.

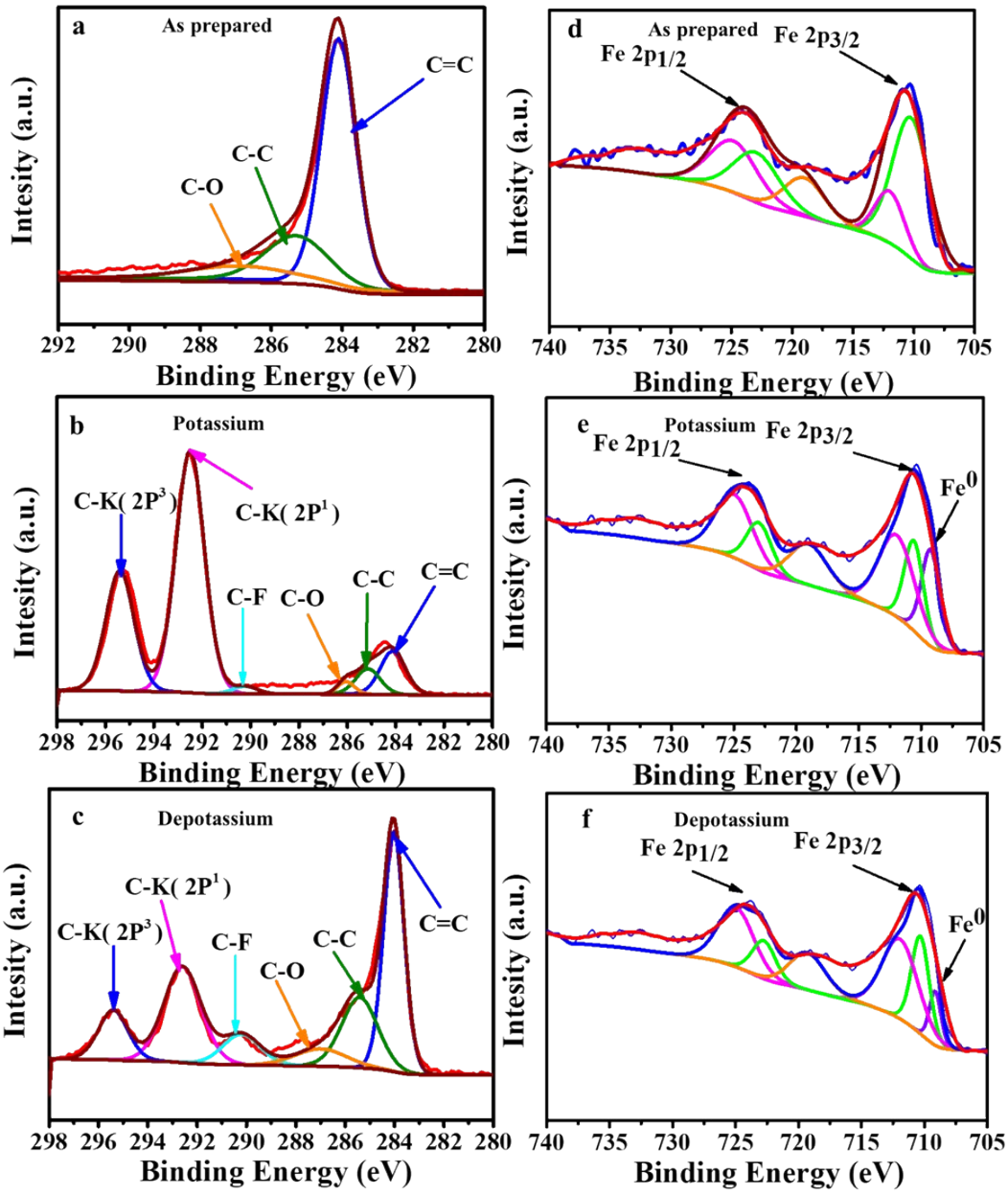

Fig. S6. *Ex-situ* XPS spectra of carbon and iron in the different valence states of Fe_3O_4@LCS-500 electrodes in KIBs. (a) carbon spectrum; (b) carbon spectrum after fully potassiated; (c) carbon spectrum after fully depotassiated; (d) iron spectrum of the as-prepared Fe_3O_4@LCS-500; (e) iron spectrum after fully potassiated; (f) iron spectrum after fully depotassiated.

To verify the redox reaction of Fe_3O_4@LCS-500 as KIB anode, *ex-situ* XPS measurements were carried out. The main peak of the carbon spectrum of Fe_3O_4@LCS-500 sample in Fig. S6a can be divided into three peaks of ~284.1, 285.6, and 286.9 eV, corresponding to C=C, C–C, and C-O, respectively. When it was fully potassiated, the peak intensity of carbon centered at 284 eV is turning weak and two new peaks emerged in Fig. S6b, relating to the C-K bonds centered at 295 eV ($2P^3$) and 292.5 eV ($2P^1$), respectively. A new peak at ~290.2 eV is associated with the formation

of the C-F bond, which is ascribed to the decomposition of electrolyte and formation of the SEI layer. After fully depotassium process, the intensities of C-K bonds are getting weaker and those C-C bonds are returned to the original state in Fig. S6c, indicating the possibility of reversible potassium-storage by carbon. Meanwhile, the XPS spectra of Fe_3O_4 in the Fe_3O_4@LCS-500 sample are displayed in Fig. S6d, which is divided into five major peaks, and similar to the analysis of LIBs. After the fully potassiated, a new peak of 709.102eV appeared in Fig. S6e, which is ascribed to the formation of metallic Fe. With the fully depotassiation (recharged) process in Fig. S6f, the intensity of Fe peak is obviously weakened, which is the solid evidence to prove the formation/disappearance of Fe, and indirectly demonstrated reversible conversion reactions of Fe_3O_4 with potassium cations for KIBs.[2]

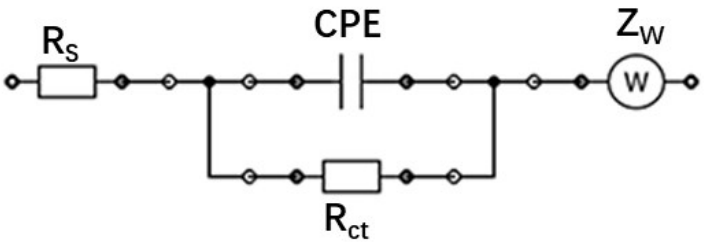

Fig. S7 The equivalent circuit model of samples (Fe_3O_4@LCS-400/500/600)

Table S2 The R*s* and R*ct* of (Fe_3O_4@LCS-400/500/600)

Material	Fe_3O_4@LCS-400 (LIBs/KIBs)	Fe_3O_4@LCS-500(LIBs/KIBs)	Fe_3O_4@LCS-600(LIBs/KIBs)
R_s/ R_{ct} for LIBs (ohm)	15.33/171.9	15.85/9.727	2.707/15.52
R_s/ R_{ct} for KIBs (ohm)	8.221/7297	7.561/4497	15.98/4999

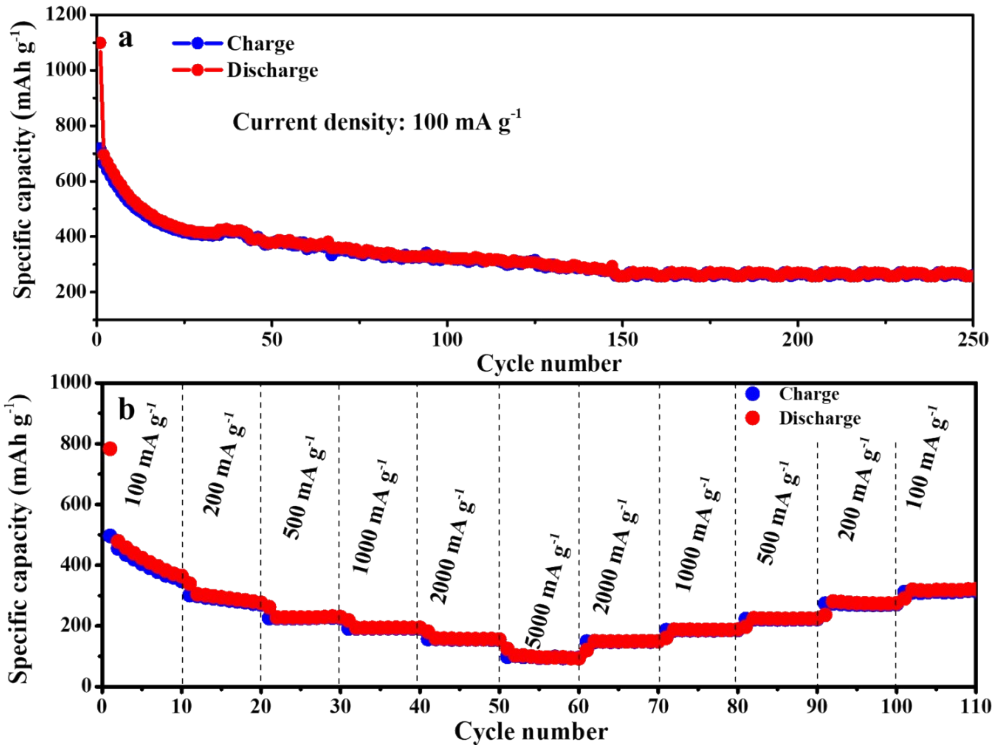

Fig. S8 Lithium storage performances of Fe_3O_4 bulk: (a) Cycle performances at 100 mA g^{-1} for 250 cycles; (b) The rate performance at various current densities.

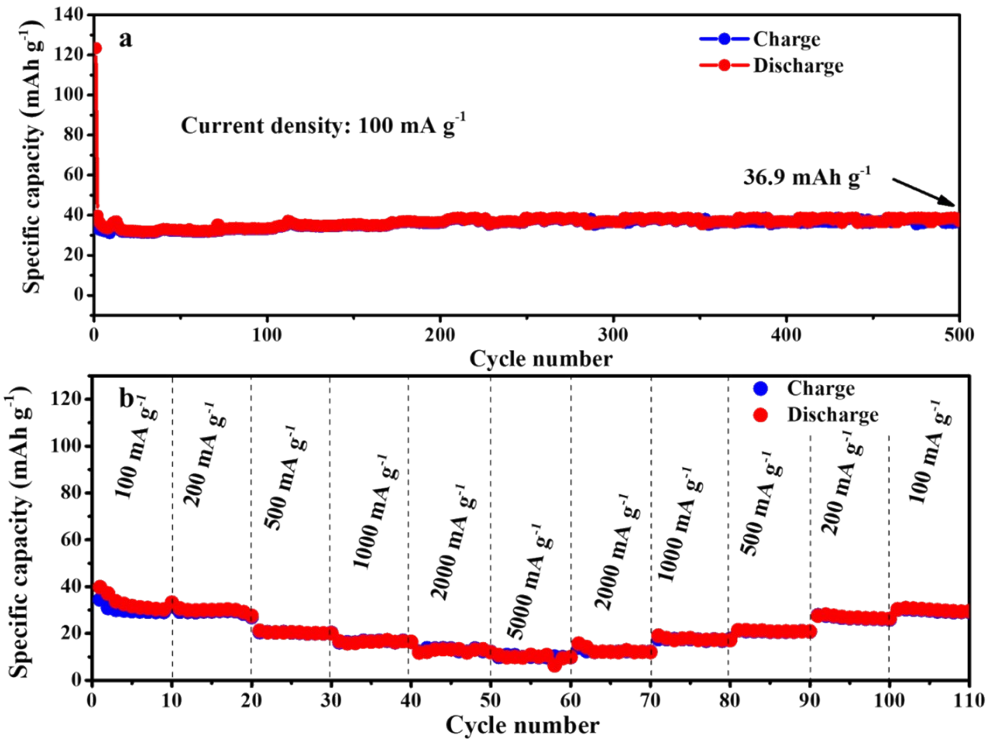

Fig. S9 The electrochemical performances of Fe_3O_4 bulk as anode of KIBs: (a) Cycle performances at 100 mA g^{-1} for 500 cycles; (b) The rate performance at various current densities.

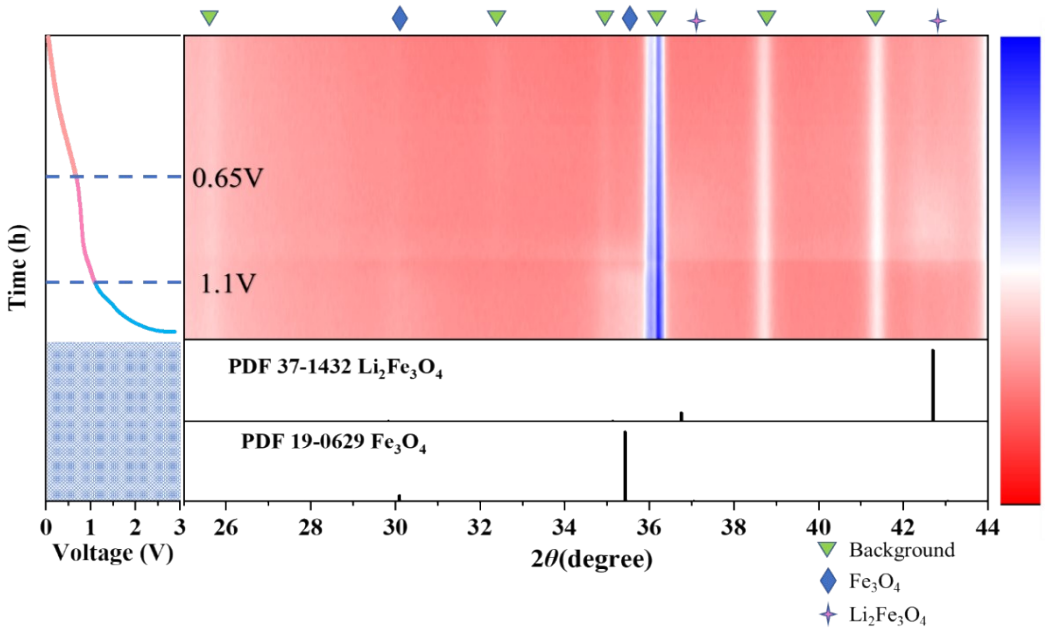

Fig. S10 *In-situ* XRD of Fe_3O_4@LCS-500 For LIBs in discharge process

A special *in-situ* XRD cell was assembled by directly coating the slurry on an ultra-thin Be foil to illustrate the generation of $Li_2Fe_3O_4$ phase. The diffraction peaks of Fe_3O_4 could be observed obviously at the initial state, and then gradually disappeared in Fig. S10. Diffraction peaks at 36.75° and 42.7°, corresponding to the (222) and (400) planes of $Li_2Fe_3O_4$, appeared when the voltage dropped to ~1.1 V, and then disappeared in following discharge process, confirming $Li_2Fe_3O_4$ was truly generated in the reduction process.

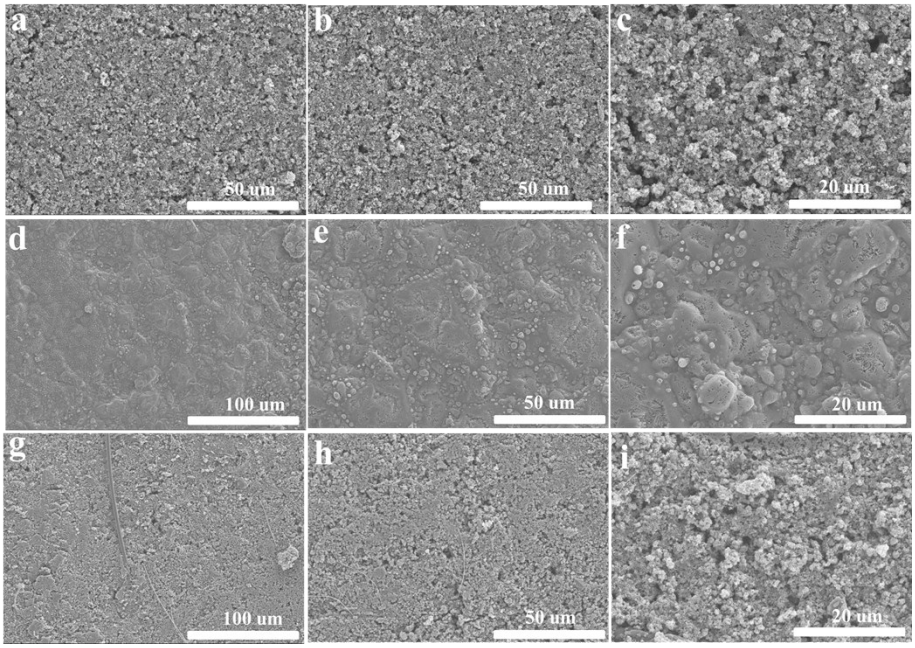

Fig. S11 SEM images of electrodes: (a-c) as prepared Fe_3O_4@LCS-500; (d-f) electrodes of Fe_3O_4@LCS-500 after 200 cycles for LIBs; (g-i) electrodes of Fe_3O_4@LCS-500 after 200 cycles for KIBs.

Table S3 Electrochemical property comparison of the Fe_3O_4@LCS electrode with previous Fe_3O_4-related electrodes.

Composite	Synthetic method	Morphology	S_{BET} (m^2 g^{-1})	V (cm^3 g^{-1})	Current density (mA g^{-1})	Cycle number	Capacity (mAh g^{-1})	References
Fe_3O_4 @ layered carbon nanosheets (Fe_3O_4@LCS)	Microwave-annealing	Nanosheet	213.84	0.60	100(LIBs) 100(KIBs) 500(KIBs) 1000(KIBs) 2000(KIBs)	250(LIBs) 500(KIBs) 1000(KIBs) 1000(KIBs) 1000(KIBs)	1126(LIBs) 429.7(KIBs) 286.8(KIBs) 260(KIBs) 141.1(KIBs)	This work
Fe_3O_4@nitrogen doped carbon nano capsule (Fe_3O_4@NC)	Hydrothermal - coating-annealing	Nanorod	74.9	/	500(LIBs) 5000(LIBs) 10000(LIBs) 20000(LIBs)	200(LIBs) 500(LIBs) 500(LIBs) 1000(LIBs)	1028(LIBs) 873(LIBs) 612(LIBs) 480(LIBs)	[1]
Fe_3O_4 dots@ carbon layer (Fe_3O_4 dots@C layers)	Oil bath- room temperature stirring-annealing	Flower-like sheet	78.1	/	500(LIBs) 1000(LIBs) 2000(LIBs)	550(LIBs) 2000(LIBs) 2000(LIBs)	1239.5(LIBs) 938.7(LIBs) 815.4(LIBs)	[2]
graphene nanosheets/Fe_3O_4 nanoparticles (GO-Fe_3O_4)	Langmuir-Schaefer (LS) technique	Oriented layered hybrid structure	/	/	1000(LIBs)	1000(LIBs)	411(LIBs)	[3]
Fe_3O_4/N-graphene sponge	Hydrothermal-freeze-dried-	Cross-linked thin graphene	154.9	/	100(LIBs)	200(LIBs)	699(LIBs)	[4]

	annealing	nanosheets						
Fe_3O_4@C nanospheres	One-step solvothermal method	Nanospheres	/	/	100(LIBs)	100(LIBs)	539(LIBs)	[5]
Mace-like carbon fibers@Fe_3O_4@carbon (CF@Fe_3O_4@C)	*In-situ* growth-carbon coating-heat treatment	Mace-like ordered structure	17.91	/	100(LIBs) 500(LIBs)	100(LIBs) 500(LIBs)	740(LIBs) 503(LIBs)	[6]
N, P and S doped dual carbon-confined Fe_3O_4 nanospheres (Fe_3O_4@C@G)	Multi-heteroatom-doped dual carbon-confined strategy	Dual carbon-confined Fe_3O_4 nanospheres	79.4	/	100(LIBs) 100(SIBs)	130(LIBs) 600(SIBs)	919(LIBs) 180(SIBs)	[7]
N-doped carbon-riveted Fe_3O_4 /N-doped carbon (N –C@Fe_3O_4@N –C)	Rational N-doped carbon riveting strategy	Fe_3O_4 /N-doped carbon tubular structures	28.41	/	100(LIBs)	100(LIBs)	675.8(LIBs)	[8]
Fe_3O_4/C nanocomposites	Nanoparticles on nanofiber aerogels	Centrifugal spinning	/	/	100(LIBs)	100(LIBs)	505(LIBs)	[9]

Fe_3O_4/reduced graphene oxide nanocomposites (Fe_3O_4/rGO)	Nanoparticles/ sheets	Gamma-irradiation method	/	/	500(LIBs)	100(LIBs)	738.5(LIBs)	[10]
1D sandwich-like C@Fe_3O_4@C coaxial nanotubes	1D sandwich-like	Bottom-up method	/	/	100(LIBs)	150(LIBs)	1087(LIBs)	[11]
Fe_3O_4@C-N yolk-shell nano capsules	Hydrothermal method/calcinate-ion	Yolk shell structure	/	/	500(LIBs)	150(LIBs)	832(LIBs)	[12]
Carbon coated Fe_3O_4 QDs imbedded on reduced graphene oxide（Fe_3O_4 QDs@C/rGO）	Water bath-Hydrothermal-annealing	Layered structure	290.43	0.4	500(LIBs) 2000(LIBs)	300(LIBs) 2000(LIBs)	737(LIBs) 505(LIBs)	[13]
Fe_3O_4 quantum dots/graphene aerogel materials（Fe_3O_4 QDs/GA）	Hydrothermal-heat treatment process	Network structure	/	/	100(LIBs)	70(LIBs)	1078(LIBs)	[14]
Fe_3O_4 quantum dots (QDs) grown on graphite paper (Fe_3O_4 QDs@MoS2-GP)	Hydrothermal-low-temperature hydrolysis-annealing	Nanosheet			100(SIBs)	300(SIBs)	388(SIBs)	[15]

Table S4 The XPS results of Fe_3O_4

Samples	XPS results of Fe	References
Fe_3O_4 @ layered carbon nanosheets (Fe_3O_4@LCS)	Fe $2p_{3/2}$ (Fe^{3+}/711.91, Fe^{2+}/710.2 eV) Fe $2p_{1/2}$ (Fe^{3+}/724.9 eV, Fe^{2+}/722.2 eV) A satellite peak (719.11 eV)	**This work**
Flower-like Fe_3O_4/C	Fe $2p_{3/2}$ (Fe^{3+}/709.8 eV, Fe^{2+}/711.3 eV) Fe $2p_{1/2}$ (Fe^{3+}/723.5 eV, Fe^{2+}/724.8 eV)	18
CF@Fe_3O_4@C	Fe $2p_{3/2}$ (711.1 eV, 720.1 eV) Fe $2p_{1/2}$ (725.0 eV, 733.7 eV)	6
N-C@Fe_3O_4 @N-C	Fe $2p_{3/2}$ (Fe^{2+}/710.9 eV) Fe $2p_{1/}$2 (Fe^{3+}/724.6 eV)	8
Fe_3O_4/C composite nanofibers	Fe $2p_{1/2}$ (723.8 eV, 733.2 eV) Fe $2p_{3/2}$(711.6 eV, 717.6 eV)	9
Fe_3O_4/rGO	Fe $2p_{3/2}$ (Fe^{3+}/712.3 eV, Fe^{2+}/710.2 eV) Fe $2p_{1/2}$ (Fe^{3+}/725.5 eV, Fe^{2+}/ 723.7 eV) The presence of Fe (III) symbiosis with Fe_3O_4 (718.3 eV and 732.4 eV)	10
Fe_3O_4@NC networks	Fe2$p_{3/2}$(710.8 eV) Fe2$p_{1/2}$(724.6 eV) a weak satellite peak (721.3 eV)	19
Fe_3O_4 QDs @C/rGO	Fe $2p_{3/2}$ (Fe^{3+}/710.0 eV, Fe^{2+}/711.8.3 eV) Fe $2p_{1/2}$ ((Fe^{3+}/723.7 eV, Fe^{2+}/725.8 eV)	13
Fe_3O_4 array	$2p_{1/2}$(724.2 eV) Fe $2p_{3/2}$ (Fe^{3+}/711.7 eV, Fe^{2+}/ 709.9 eV) The fingerprint of γ-Fe_2O_3(719 eV)	20
Fe_3O_4/N-GAs	Fe $2p_{3/2}$(711 eV) Fe2$p_{1/2}$(725 eV),	21
Sandwich-like C/Fe_3O_4/rGO	Fe $2p_{3/2}$ (Fe^{3+} /711.7, Fe^{2+}/ 710.3 eV, 710.6 eV) Fe $2p_{1/2}$ (Fe^{3+}/725.1 eV, Fe^{2+}/723.6 eV, 724.5 eV)	22

Reference

1. L. Wan, D. Yan, X. Xu, J. Li, T. Lu, Y. Gao, Y. Yao and L. Pan, *J. Mater. Chem. A*, 2018, **6**, 24940-24948.
2. Q. Li, H. Li, Q. Xia, Z. Hu, Y. Zhu, S. Yan, C. Ge, Q. Zhang, X. Wang, X. Shang, S. Fan, Y. Long, L. Gu, G. X. Miao, G. Yu and J. S. Moodera, *Nat. Mater*, 2020, DOI: 10.1038/s41563-020-0756-y.
3. H. Duan, S. Zhang, Z. Chen, A. Xu, S. Zhan and S. Wu, *ACS Applied Materials & Interfaces*, 2020, **12**, 527-537.
4. Z. Shi, Q. Zhang, L. Zhao, H. Wang and W. Zhou, *ACS Applied Materials & Interfaces*, 2020, **12**, 15043-15052.
5. H.-S. Jeong, H. Kim, K.-I. Jo, J. Jang, J.-H. Choi and J. Koo, *Applied Surface Science*, 2020, **508**, 144416.
6. J. He, A. Bhargav and A. Manthiram, *Energy Storage Materials*, 2019, **23**, 88-94.
7. H. Lv, *International Journal of Electrochemical Science*, 2020, DOI: 10.20964/2020.03.21, 2157-2165.
8. S. Yao, G. Zhang, X. Zhang and Z. Shi, *Ionics*, 2020, DOI: 10.1007/s11581-020-03748-6.
9. X. Tao, Y. Li, H.-G. Wang, X. Lv, Y. Li, D. Xu, Y. Jiang and Y. Meng, *Journal of Colloid and Interface Science*, 2020, **565**, 494-502.
10. T. Ma, X. Liu, L. Sun, Y. Xu, L. Zheng and J. Zhang, *Journal of Energy Chemistry*, 2019, **34**, 43-51.
11. M. Akia, N. Salinas, S. Luna, E. Medina, A. Valdez, J. Lopez, J. Ayala, M. Alcoutlabi and K. Lozano, *Journal of Materials Science*, 2019, **54**, 13479-13490.
12. Y. Liang and W. Lu, *Journal of Materials Science: Materials in Electronics*, 2020, DOI: 10.1007/s10854-020-04268-9.
13. Q. Qu, J. Chen, X. Li, T. Gao, J. Shao and H. Zheng, 2015, **3**, 18289-18295.
14. Q. Wu, R. Zhao, W. Liu, X. Zhang, X. Shen, W. Li, G. Diao and M. Chen, 2017, **344**, 74-84.
15. C. Wang, S. Mutahir, L. Wang, W. Lei, X. Xia, X. Jiao and Q. Hao, *Applied Surface Science*, 2020, **509**, 144882.
16. Y. Wang, Y. Jin, Y. Duan and M. Jia, *Ionics*, 2017, **23**, 2005-2011.
17. D. Kong, C. Cheng, Y. Wang, Z. Huang, B. Liu, Y. Von Lim, Q. Ge and H. Y. Yang, *Journal of Materials Chemistry A*, 2017, **5**, 9122-9131.
18. L. Wan, D. Yan, X. Xu, J. Li, T. Lu, Y. Gao, Y. Yao and L. Pan, *Journal of Materials Chemistry A*, 2018, **6**, 24940-24948.
19. C. Mao, X. Xu, S. Wang, J. Liu, X. Guo, H. Peng, Z. Zhang and G. Li, *Applied Surface Science*, 2020, **505**, 144525.
20. G. Zhong, K. Qu, C. Ren, Y. Su, B. Fu, M. Zi, L. Dai, Q. Xiao, J. Xu, X. Zhong, F. An, M. Ye, S. Ke, S. Xie, J. Wang, P. Gao and J. Li, *Nano Energy*, 2020, **74**, 104876.
21. Z.-S. Wu, S. Yang, Y. Sun, K. Parvez, X. Feng and K. Müllen, *Journal of the American Chemical Society*, 2012, **134**, 9082-9085.
22. Q. Wu, R. Jiang and H. Liu, *Ceramics International*, 2020, **46**, 12732-12739.